npj | Computational Materials

www.nature.com/npjcompumats

ARTICLE OPEN

Check for updates

Field-free spin–orbit torque perpendicular magnetization switching in ultrathin nanostructures

Minyi Dai[1] and Jia-Mian Hu[1]✉

Magnetic-field-free current-controlled switching of perpendicular magnetization via spin–orbit torque (SOT) is necessary for developing a fast, long data retention, and high-density SOT magnetoresistive random access memory (MRAM). Here, we use both micromagnetic simulations and atomistic spin dynamics (ASD) simulations to demonstrate an approach to field-free SOT perpendicular magnetization switching without requiring any changes in the architecture of a standard SOT-MRAM cell. We show that this field-free switching is enabled by a synergistic effect of lateral geometrical confinement, interfacial Dyzaloshinskii–Moriya interaction (DMI), and current-induced SOT. Both micromagnetic and atomistic understanding of the nucleation and growth kinetics of the reversed domain are established. Notably, atomically resolved spin dynamics at the early stage of nucleation is revealed using ASD simulations. A machine learning model is trained based on ~1000 groups of benchmarked micromagnetic simulation data. This machine learning model can be used to rapidly and accurately identify the nanomagnet size, interfacial DMI strength, and the magnitude of current density required for the field-free switching.

npj Computational Materials (2020)6:78 ; https://doi.org/10.1038/s41524-020-0347-0

INTRODUCTION

Magnetization switching through spin–orbit torque (SOT) is of great recent interests due to its potential applications in SOT magnetoresistive random access memory (SOT-MRAM), which is expected to have faster write speed, lower write energy, and higher endurance than the currently used spin-transfer torque MRAM[1,2]. An SOT-MRAM cell integrates a magnetic tunnel junction (MTJ) on top of a heavy-metal layer. During writing, an in-plane charge current flowing into the heavy-metal layer is converted to a perpendicular spin current via the spin Hall effect (SHE)[3–5], as schematically shown in Fig. 1a. The spin current then flows into the overlaying magnetic layer and switch its magnetization via the SOT. SOT has been used to switch both the perpendicular[6] and in-plane[7] magnetization, but perpendicular switching is more attractive for SOT-MRAM applications because it is faster[8] and more scalable[9]. However, SOT-mediated perpendicular magnetization switching typically requires a simultaneous application of an in-plane bias magnetic field[6,7]. This in-plane magnetic field is not desirable for practical SOT-MRAM application, because it reduces the thermal stability of perpendicular magnetization and because it may cause crosstalk among neighboring SOT-MRAM cells. .

Thus far, many approaches have been proposed for achieving a magnetic-field-free SOT-mediated perpendicular magnetization switching. An early proposed approach is to fabricate asymmetric multilayer stack, such as engineering a thickness gradient into the magnetic layer[10] or its overlaying oxide[9] or heavy-metal layer underneath[11]. Such structural asymmetry generates a unidirectional effective perpendicular magnetic field, leading to a deterministic switching. Approaches proposed thereafter aim to introduce a built-in in-plane bias magnetic field, generated by an in-plane magnetized reference layer in the MTJ[12,13] or an antiferromagnetic heavy-metal with in-plane magnetized sublattices[14]. Other approaches include (1) adding a ferroelectric layer below the heavy-metal to harness the effect of electric-field-switchable spontaneous polarization[15] or piezoelectric strain[16]; (2) adding another heavy-metal layer to generate competing spin currents[17]; (3) applying an out-of-plane charge current from the top terminal of the MTJ to generate an assisting STT[18]; and (4) engineering the geometry of the ferromagnetic layer[19,20]. Most recently, micromagnetic simulations[21,22] have suggested that a magnetic-field-free SOT perpendicular magnetization switching can also be achieved by simultaneously controlling the lateral size of the magnetic layer, the strength of the Dyzaloshinskii–Moriya interaction (DMI) arising from the ferromagnet/heavy-metal interface, and the magnitude of applied charge current density within an intermediate range. Compared with earlier proposed approaches, this approach does not require any changes in the architecture of a standard perpendicular SOT-MRAM cell, which is important to practical applications.

In this article, we use both micromagnetic and atomistic spin dynamics (ASD) simulations (see "Methods") to study the nucleation of the reversed magnetic domain and its subsequent growth during the two-step switching. Notably, the ASD model enables predicting the evolution of atomistic spin moment of each atom based on the actual lattice structure of the material, which leads to a generally more accurate description of the nucleation process, especially at its early stage when embryos (clusters of several atoms) are too small to be accurately described by micromagnetic model. We show that the lateral geometrical confinement, interfacial DMI, and current-induced SOT synergistically lead to a deterministic nucleation and growth process. Accordingly, it is found that the field-free SOT perpendicular switching occurs when the lateral size of the nanomagnet, the interfacial DMI strength, and the magnitude of applied current are all within an intermediate range. Furthermore, a decision-tree-based machine learning model is trained using data from about 1000 groups of benchmarked micromagnetic simulations, which is then used to rapidly and accurately identify the regime of successful two-step switching from a ternary parameter space comprising the lateral size of magnetic layer, interfacial DMI strength, and magnitude of charge current density.

[1]Department of Materials Science and Engineering, University of Wisconsin–Madison, Madison, WI 53705, USA. ✉email: jhu238@wisc.edu

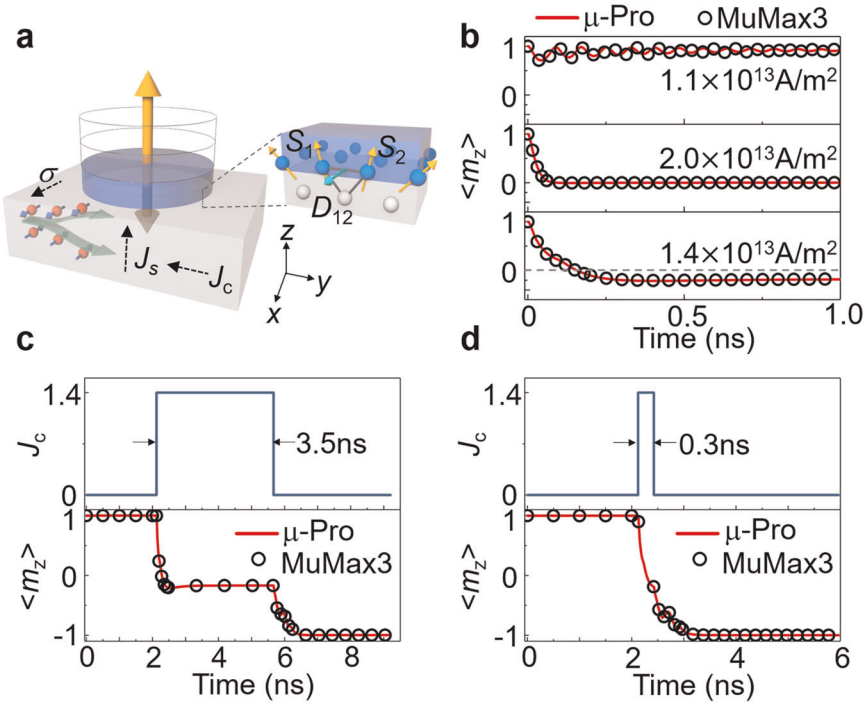

Fig. 1 Field-free SOT perpendicular switching in a standard SOT-MRAM cell. a Schematic of the SOT-MRAM cell which integrates a magnetic tunnel junction (e.g., CoFeB/MgO/CoFeB) on a heavy-metal layer. The simulations consider a 40 nm diameter MgO/$Co_{20}Fe_{60}B_{20}$(1.1 nm) bilayer nanodisks on top of a Pt layer. The Pt layer converts the in-plane charge current J_c to an out-of-plane spin current J_s via the spin Hall effect. The Dyzaloshinskii–Moriya interaction at the $Co_{20}Fe_{60}B_{20}$/Pt interface (sketched on the right) induces tilted perpendicular magnetization vector along the disk edge. **b** Temporal evolution of the average perpendicular magnetization $<m_z>$ under time-invariant J_c of different magnitudes, where the $<m_z>$ equilibrates with a negative value when J_c is at the intermediate value of 1.4×10^{13} A/m^2. Full perpendicular reversal ($<m_z>$ changes from 1 to −1, or vice versa) driven by a pulsed current J_c of the same magnitude but different durations: 3.5 ns in **c** and 0.3 ns in **d**. Data in **b**–**d** were obtained using both the commercial μ-Pro® package and the open-source package MuMax3.

RESULTS

Field-free SOT perpendicular switching in a standard SOT-MRAM cell

Consider a 40 nm diameter MgO/$Co_{20}Fe_{60}B_{20}$(1.1) bilayer nanodisks on top of a Pt layer as an example. Figure 1b shows the evolution of the average perpendicular magnetization $<m_z>$ of the 1.1-nm-thick $Co_{20}Fe_{60}B_{20}$ (CoFeB) nanodisk under a time-invariant current J_c, simulated using both the μ-Pro and MuMax3 software (see "Methods"). The interfacial DMI strength D is set to be 0.45 mJ/m^2 based on experimental measurement[23]. When J_c is relatively small (top panel of Fig. 1b), the SOT is insufficient to rotate the initially upward magnetization significantly. When J_c is large (middle panel), the SOT is large enough to switch the magnetization by 90° to the direction of net spin polarization σ (which is along the $+x$-axis, see Fig. 1a). This is consistent with the conventional belief that the SOT alone typically cannot reverse the polarity of an out-of-plane magnetization due to the inability to break mirror symmetry[9]. However, an unconventional SOT switching appears under a moderate magnitude of current, showing a reversal of the out-of-plane magnetization component. As shown in the bottom panel of Fig. 1b, $<m_z>$ equilibrates at a negative value (approximately −0.17) under $J_c = 1.4 \times 10^{13}$ A/m^2. This indicates that a majority portion of local magnetization vectors were flipped from up to down, and thereby provides a basis for realizing a two-step switching under a pulsed charge current. Specifically, if turning off the current when $<m_z>$ equilibrates at 3.5 ns after turning on the current (see Fig. 1c) or evolves to its lowest negative value (at 0.3 ns, see Fig. 1d), the magnetization state will deterministically relax to its new equilibrium state with a downward magnetization ($<m_z>$ approximately −1).

Deterministic > 90° perpendicular switching under a time-invariant current

Thus, flipping a major portion (>50%) of local magnetization vectors from up to down (and vice versa) in a deterministic manner using SOT is the basis for the two-step switching, and is called ">90° switching" hereafter for convenience. Figure 2a–d shows the local magnetization distributions at several key time stages, including the initially upward magnetization with tilted vectors along the disk edges (0 ns), where the tilting occurs due to the co-action of interfacial DMI and lateral geometrical confinement (ref.[24], also see "Methods"); the nucleation of downward domain (0.07 ns); the critical state at which $<m_z> \sim 0$ (0.18 ns), and the equilibrium state (0.71 ns), all under the time-invariant J_c of 1.4×10^{13} A/m^2. Starting from the initially quasiuniform state where inwards tilting edge magnetization, the domain nucleation always occurs in the bottom left region (the third quadrant) of the disk under a J_c flowing along the $-y$ direction. This is because only in this region, the out-of-plane SOT τ_z^{SOT} and the out-of-plane SHE effective field H_z^{SOT} are both negative (as shown in Fig. 2f and explained in "Methods"). Such a nucleation mechanism is similar to that in a conventional SOT perpendicular magnetization reversal in the presence of in-plane bias magnetic field[25–27]. However, the growth kinetics of the downward domain we present herein under zero magnetic field (Fig. 2b–d) is different. Specifically, the curvature of the domain wall changes from an initially negative value (Fig. 2b) to almost zero when $<m_z> \sim 0$ (Fig. 2c), and then to a positive value (Fig. 2d). Figure 2e shows the trajectories of the domain wall motion during the entire process of >90° switching. It can be seen that the growth of downward domain is more favorable in the second and third quadrants of the disk, which is due to the fact that the out-of-plane SOT τ_z^{SOT} is

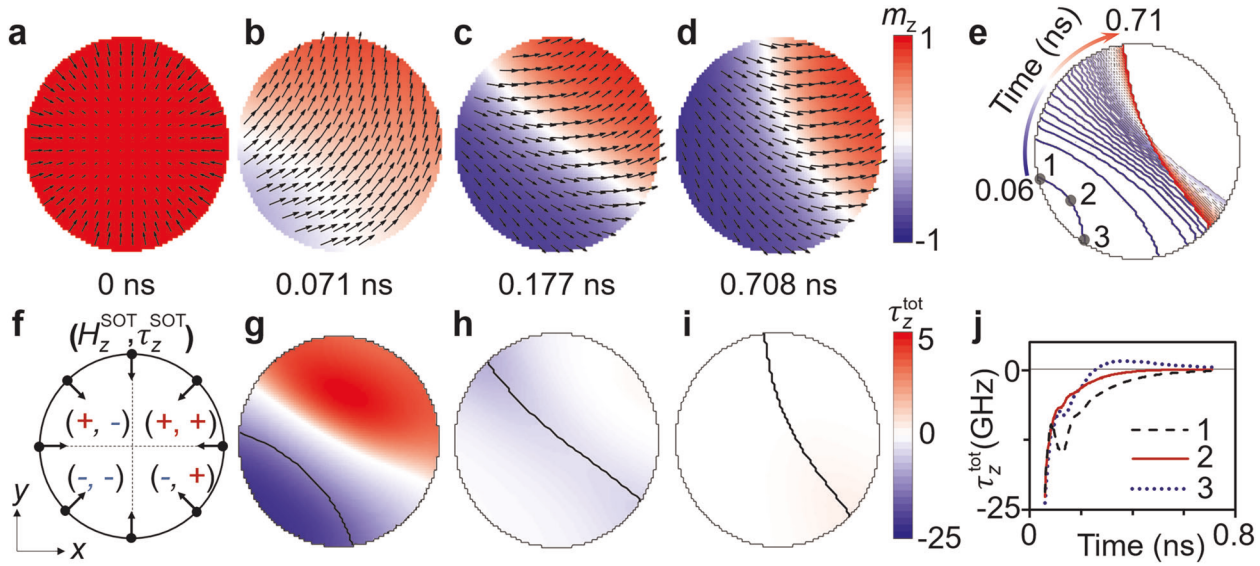

Fig. 2 Key step: a deterministic ">90° perpendicular switching". Top-view magnetization distributions of the 1.1-nm-thick, 40 nm diameter $Co_{20}Fe_{60}B_{20}$ disk at **a** the initial state (0 ns) and **b**–**d** later time stages, under a time-invariant charge current density $J_c = 1.4 \times 10^{13}$ A/m^2. The arrows indicate the direction of the normalized in-plane magnetization vectors. **e** Trajectories of domain wall motion from the beginning of nucleation (0.06 ns) to the equilibrium (0.71 ns), plotted with a time stepping of 0.012 ns. **f** Schematic of the in-plane components of the inward tilted edge magnetization at 0 ns. The signs of the perpendicular SHE effective field H_z^{SOT} and the perpendicular Slonczewski-type SOT τ_z^{SOT} (Eq. 2) in each quadrant of the disk are indicated. The nucleation of downward domain occurs in the third quadrant, in which both H_z^{SOT} and τ_z^{SOT} are negative, see for example the magnetization distribution at **b**. **g**–**i** Top-view distributions of the total torque τ_z^{tot} corresponding to the evolving magnetization distributions shown in **b**–**d**. **j** Evolution of the total torque τ_z^{tot} at the two ends of the domain wall (point "1" and "2" in **e**) and center wall position (point "3").

negative in both regions (see Fig. 2f). For further analysis, the evolution of the total out-of-plane torque τ_z^{tot} are plotted. The spatial distributions of τ_z^{tot} in the entire disk are shown in Fig. 2g–i, while the evolution of site-specific τ_z^{tot} along the domain wall is shown in Fig. 2j. Two key observations are noted. First, the τ_z^{tot} is negative in the front of the domain walls for most of the time during the wall motion, which is mainly because the out-of-plane SOT torque τ_z^{SOT} in front of the domain wall is always negative (see complete torque analysis in Supplementary Fig. 1). This negative τ_z^{SOT} can be inferred from its formula $\tau_z^{SOT} = -\gamma_0 H_0 m_x m_z$, where (1) the local m_x is always positive during the wall motion (see Fig. 2b–d) to maintain the left-chirality of the domain wall (caused by the positive interfacial DMI strength D); (2) the local m_z is always positive in front of the domain wall (which is the unswitched area); and (3) γ_0 is positive and the coefficient H_0 is positive under a positive J_c (see "Methods"). Since the total out-of-plane torque τ_z^{tot} is negative in front of the wall, local magnetization vectors therein rotate deterministically from up to down. As a result, the domain wall moves forwards in a unidirectional manner and drives the magnetization distribution across the critical state of $<m_z> \sim 0$ (Fig. 2c). Second, for most of the time, the τ_z^{tot} at the two ends of the domain wall (point "1" and "3" in Fig. 2e) are larger than that in the center (point "2"), leading to the formation of a positive domain wall curvature at equilibrium.

Repeatable 180° perpendicular switching induced by either unipolar or bipolar current pulses

The above analyses show that the nucleation and growth of the downward domain during the >90° switching (step 1) and the subsequent relaxation to $<m_z>$ approximately −1 (step 2) are both deterministic. We note that achieving such a two-step SOT perpendicular switching does not require the breaking of mirror symmetry. This feature allows for switching a perpendicular magnetization repeatedly with either a unipolar or bipolar (Supplementary Fig. 2) current pulse, which is not possible to achieve with other field-free SOT switching approaches and therefore adds flexibility in the way of writing information. Figure 3a shows the evolution of both the $<m_z>$ and the total magnetic free energy density change Δf_{tot} (see "Methods") under a unipolar current pulse. As seen, the forward switching (up to down, $<m_z>$ changing from 1 to −1) and the backward switching (down to up, $<m_z>$ changing from −1 to 1) show exactly the same profile of $\Delta f_{tot}(t)$. As seen from the zoom-in view of $\Delta f_{tot}(t)$ in Fig. 3b, for both the forward and backward switching, the realization of the >90° switching (step 1) requires overcoming an energy density barrier for the nucleation of an oppositely oriented domain and another barrier (albeit small for this particular case) for pushing the domain wall forward at the critical state of $<m_z> \sim 0$, both driven by the out-of-plane SOT torque τ_z^{SOT} as discussed above. Figure 3c shows the magnetization distributions at the initial and final stage of the switching as well as the two transitional states (where Δf_{tot} peaks). It can be seen that the evolution of magnetization distributions during backward switching is symmetric to that in the forward switching. This explains why the free energy evolution during the backward switching is exactly the same as that in forward switching as shown in Fig. 3b. However, for the backward switching, the magnetization is initially pointing down and the edge magnetization tilts outwards due to the interfacial DMI, which is exactly opposite to the initial state in the case of forward switching. Therefore, the domain nucleation occurs at the bottom right region (the fourth quadrant) of the disk where the out-of-plane SOT τ_z^{SOT} and the out-of-plane SHE effective field H_z^{SOT} are both positive since the polarity of the current J remains unchanged. Likewise, the growth of upward domain is more favorable in the fourth and the first quadrants where the τ_z^{SOT} is positive.

DISCUSSIONS

Below we show that achieving a >90° out-of-plane SOT switching under a time-invariant current requires a balanced combination of the geometrical confinement (disk diameter), interfacial DMI

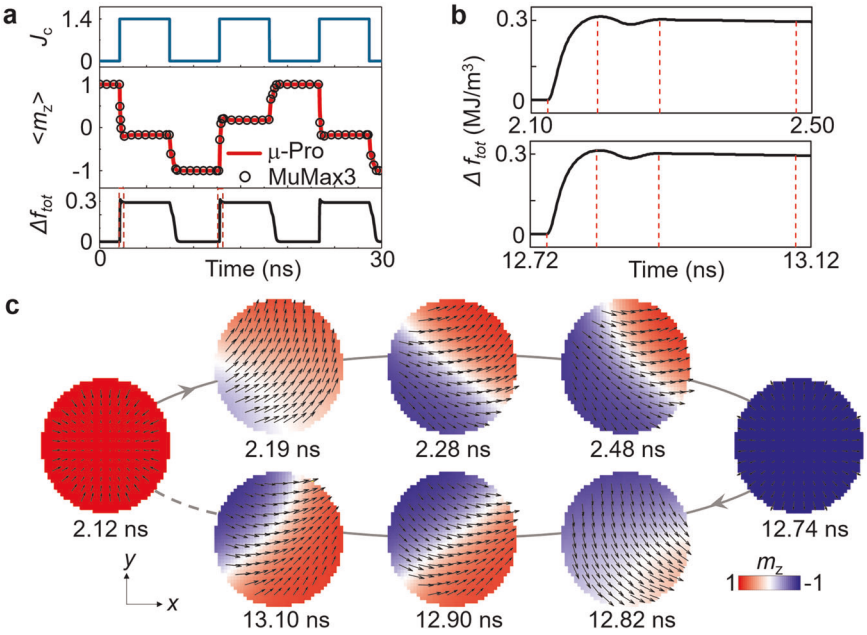

Fig. 3 180° perpendicular magnetization switching induced by unipolar current pulses. a The evolution of both the $<m_z>$ and the total magnetic free energy density change Δf_{tot} (see "Methods") in a 1.1-nm-thick; 40 nm diameter $Co_{20}Fe_{60}B_{20}$ disk. A unipolar current pulse (magnitude: 1.4×10^{13} A/m^2; duration: 5.31 ns) is applied to the Pt underlayer. **b** zoom-in view of the $\Delta f_{tot}(t)$ when $<m_z>$ changes from ~1 to −0.21 (upper panel), and when $<m_z>$ changes from approximately −1 to 0.21 (lower panel). **c** Magnetization distributions at several key stages, all indicated by vertical dashed lines in (**b**). These include the initial and final stage of the forward ($<m_z>$ changes from approximately 1 to approximately −1) and backward ($<m_z>$ changes from approximately −1 to approximately 1) switching; the two transitional states (where Δf_{tot} peaks), corresponding to the beginning of the reversed domain nucleation (2.19 ns for the forward switching and 12.82 ns for the backward switching) and the critical stage where the domain wall has an almost zero curvature (2.28 and 12.90 ns for the forward and backward switching, respectively); the equilibrium state of the >90° switching. The arrows indicate the direction of the normalized in-plane magnetization vectors, respectively. Data in **a** and **b** were obtained using both the commercial μ-Pro® package and the open-source package MuMax3.

(strength D), and SOT (magnitude of charge current J_c). Let us first discuss the role of confinement under a constant D of 0.45 mJ/m^2, which is an experimentally measured value for CoFeB/Pt interface[23]. Figure 4a shows the switching diagram as a function of disk diameter and J_c, where the region of successful switching is colored by the equilibrium value of $<m_z>$. It can be seen that the desirable >90° switching appears not only within an intermediate range of J_c (as have shown in Fig. 1b) but also an intermediate range of disk diameter (40–63 nm). At smaller disk diameters, the CoFeB disk has a larger perpendicular magnetic anisotropy (PMA), defined as $K_{PMA} = \frac{K_{inter}}{d} + K_{shape}^{OOP}$. Here, K_{inter} is the magnetic interfacial anisotropy (~1.3 mJ/m^2 for CoFeB)[28] and d is the disk thickness; the out-of-plane magnetic shape anisotropy K_{shape}^{OOP} is larger in smaller disks due to stronger geometrical confinement (see "Methods"). The enhanced PMA facilitates the alignment of magnetization along the z-axis, thereby reducing the extent of interfacial-DMI-induced magnetization tilting along the disk edge. As shown in Fig. 4b, the magnitude of the normalized in-plane magnetization m_{IP} along the disk edge (see schematic in the inset) decreases as the disk diameter reduces. This in turn makes it harder for the reversed domain to nucleate due to the smaller τ_z^{SOT} and H_z^{SOT}[25,26], demonstrated by the larger threshold J_c. This trend continues until m_{IP} becomes smaller than a threshold (~7.22×10^{-2}), below which the nucleation of reversed domain is not possible. As the disk diameter increases, m_{IP} also increases and gradually approaches its saturation value (~7.31×10^{-2}). The latter is linearly proportional to D[24]. A larger m_{IP} will make it easier for the reversed domain to nucleate and hence facilitate the >90° switching, demonstrated by the decreasing J_c as well as a more negative $<m_z>$ at equilibrium (Fig. 4a). However, the volume fraction of the tilted edge magnetization (denoted as V_t, see inset of Fig. 4b) decreases with increasing disk diameter, because the interfacial DMI primarily tilts magnetization along the outermost edge of the disk. When V_t becomes smaller than a threshold (~10.88%), the domain nucleation is also disabled, in other words, the numbers of flipped magnetization vectors are too small to trigger a nucleation. This is analogous to a classical nucleation process where the size of the unstable embryo cluster cannot grow large enough to exceed the critical nucleus size.

Furthermore, the fact that there exists a lower and an upper bound for the disk diameter suggests that the desirable >90° perpendicular SOT switching may be more robust when the disk diameter is far away from the two bounds. In that case, both the m_{IP} and V_t can maintain a sufficiently large value, which synergistically facilitate the nucleation and thereby lead to a more robust switching. To test this hypothesis, we compared the success rate of the switching in the presence of a thermal fluctuation field at room temperature (see "Methods") for the cases of 40, 50, and 60 nm based on 100 groups of repeated simulations for each case. It is found that the success rate in the case of 50 nm is as high as 98%, which is much higher than that in the case of 40 nm (50%) and 60 nm (54%) (see Supplementary Fig. 3). In this regard, the switching diagram in Fig. 4a allows us to infer the robustness of the switching under other combinations of current densities and disk diameters. We also note that this finding (that is, higher success rate in an intermediate disk size) is different from the perpendicular magnetization switching driven by current-induced spin-transfer torques[28] or voltage-controlled magnetic anisotropy[29,30], where the switching in larger-volume single-domain nanomagnets generally has a higher success rate due to the enhanced thermal stability[31,32].

Figure 4c shows the switching diagram as a function of the interfacial DMI strength D and the J_c under a constant disk

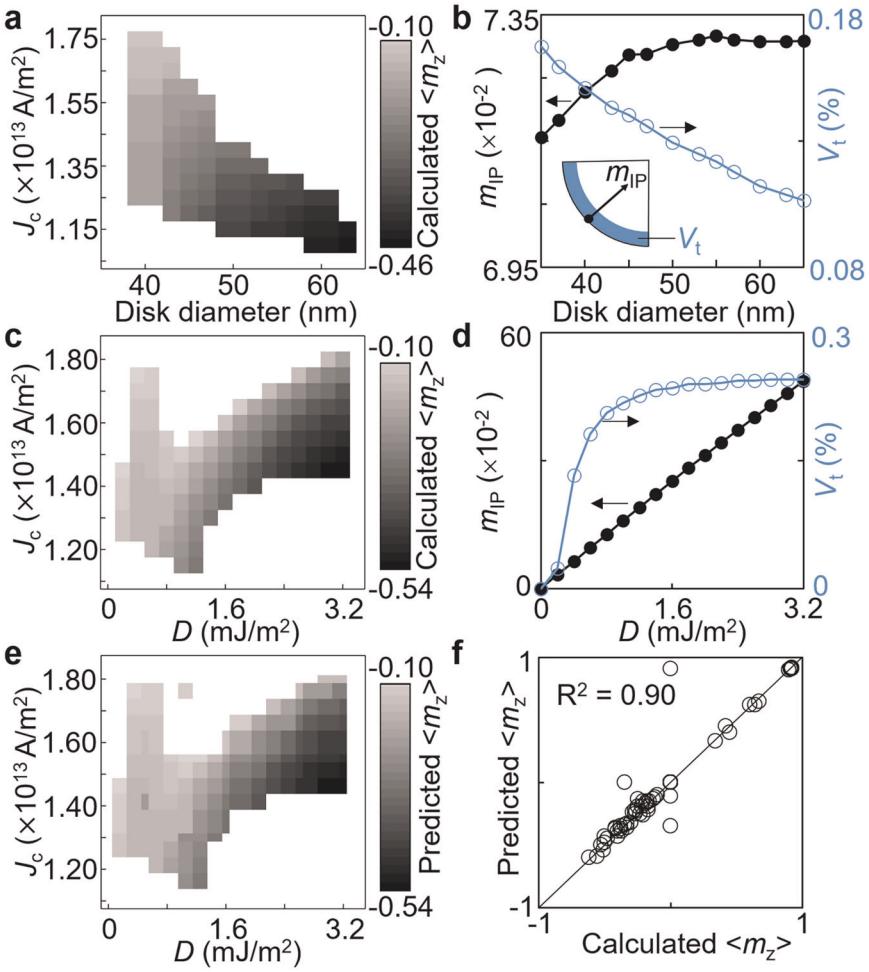

Fig. 4 Synergistic effect of confinement, interfacial DMI, and SOT enables the deterministic > 90° perpendicular switching. a The switching diagram of equilibrated value of $<m_z>$ as a function of the disk diameter and the charge current density J_c with a constant interfacial DMI strength (D) of 0.45 mJ/m^2. **b** The magnitude of the normalized in-plane magnetization along the disk edge m_{IP} and the volume fraction of the tilted edge magnetization V_t at the initial stage of the switching (i.e., before applying currents) in $Co_{20}Fe_{60}B_{20}$ disks of different diameters. **c** The switching diagram as a function of the interfacial DMI strength D and the charge current density J_c with a constant disk diameter of 40 nm. **d** The m_{IP} and V_t at the initial stage of the switching as a function of D. **e** The switching diagram for the disk diameter of 40 nm predicted by machine learning, in comparison with the diagram in **c**. **f** Machine-learning-predicted $<m_z>$ against calculated $<m_z>$ for 80 groups of tests. The prediction accuracy of the machine learning model, trained with 989 groups of data points, is ~90% (represented by R^2 score).

diameter of 40 nm. As seen, the desirable >90° switching only appears within an intermediate range of DMI strength D (0.2–3.2 mJ/m^2) and an intermediate range of J_c. When D is relatively small (≤1 mJ/m^2), increasing D reduces the J_c. This is because the resultant increase in both the m_{IP} and V_t, as shown in Fig. 4d, reduces the energy density barrier for the nucleation of revered domain (Supplementary Fig. 4). However, when D is relatively large (1.2 mJ/m^2 ≤ D ≤ 3.2 mJ/m^2), increasing D increases the J_c, despite that both the m_{IP} and the V_t still increase. We attribute the larger J_c to the change in the domain wall structure and the kinetic switching path when D is relatively large (Supplementary Fig. 5). Specifically, a large D tends to destabilize both the initial upward (downward) magnetization[33] and the domain wall, thereby making the domain wall motion more turbulent (Supplementary Video 1) which in turn reduces the mobility of the domain wall[34,35]. As a result, a larger J_c will be required to move the domain wall. This is reminiscent of the Walker breakdown for the magnetic field or current-induced motion of 180° magnetic domain walls, where domain wall exhibits lower mobility if the field or current is so large that the domain wall structure becomes less stable during motion[36,37]. When D is even larger (≥3.4 mJ/m^2), the equilibrium spin structure under an intermediate J_c displays an almost pure Néel wall that separates upward and downward domains (note that mixed Néel and Bloch wall features appear at lower D values). Once the current is turned off, this spin structure will relax to a metastable or stable (if D is sufficiently large[33]) Néel stripe domain, where upward and downward domains are roughly half and half with $<m_z>$ ~ 0 (Supplementary Fig. 6), rather than relaxing to the desirable downward single-domain with $<m_z>$ approximately −1.

We also simulated the J_c vs. D switching diagrams for other disk diameters in the range of 40–63 nm. It is found that the switching diagrams in the cases of other disk diameters all exhibit two features that are the same as the above-discussed 40 nm diameter case, due to similar physical mechanisms. First, as D increases, the critical J_c required for the >90° switching decreases (increases) when D is relatively small (large). Second, the relaxation to single domain of reversed polarity in the second step is prohibited if D is too large. The numerical calculation of such switching diagram is tedious because one needs to search for the desirable range of J_c for each combination of D and disk diameter. To accelerate the calculation of switching diagram, we

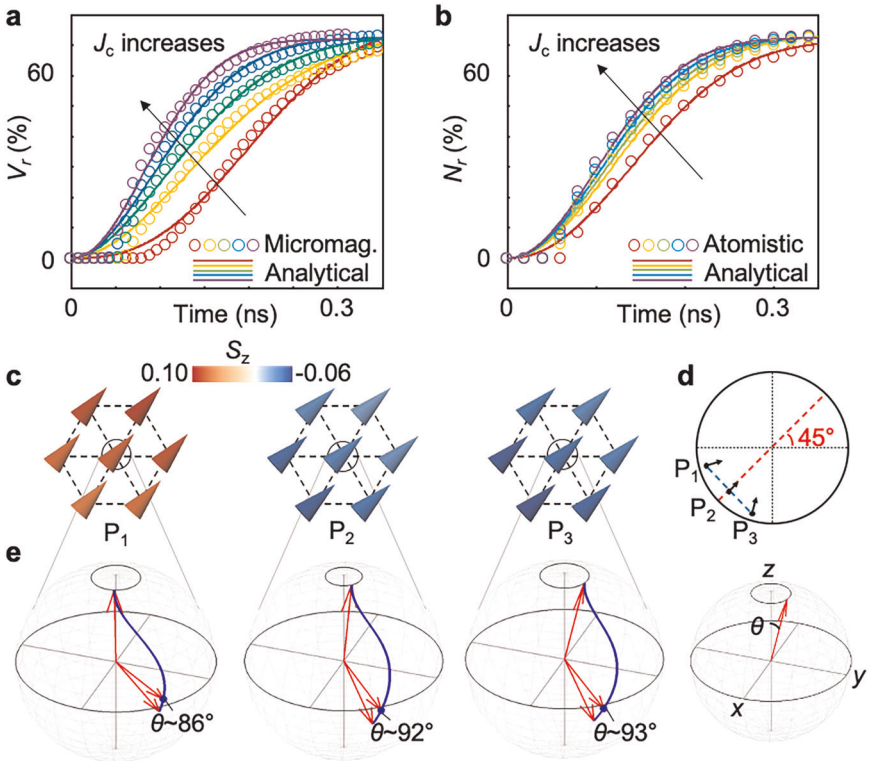

Fig. 5 On the kinetics of reversed domain nucleation and growth during the >90° perpendicular magnetization switching. Both the **a** micromagnetic and **b**–**e** atomistic spin dynamics (ASD) simulations consider a 50 nm diameter MgO/Co(1.1 nm) bilayer nanodisks on top of a Pt layer. **a** Volume fraction of the reversed domain (regions where $m_z < 0$) as a function of time, calculated from micromagnetic simulations. J_c increases from 1.1×10^{13} to 1.5×10^{13} A/m^2. **b** Percentage of atoms with flipped magnetization ($S_z < 0$) as a function of time, calculated from ASD simulations. J_c increases from 4.5×10^{12} to 5.0×10^{12} A/m^2. In both **a** and **b**, the growth kinetics of the reversed domain well fits the Kolmogorov–Avrami equation (results plotted using lines). **c** Distributions of the normalized perpendicular atomic spin moment S_z in three different nucleation clusters P_1, P_2, and P_3 (indicated in **d**) at the same time stage of 0.055 ns. The central atoms are marked by circles (whose radii are not to scale with the atomic radius of cobalt). The lattice parameter of the hexagonal lattice is 0.25 nm. **e** The evolution trajectories of the normalized atomic spin moment of these three central atoms from 0 ns (at which $S_z \sim 1$) to 0.06 ns (at which $S_z < 0$). The schematic in the right shows the polar angle θ of the normalized atomic spin moment.

train a decision-tree-regression-based machine learning model (see "Methods") from about 1000 groups of micromagnetic simulation datasets. The machine learning model is then tested with 80 datasets. Each dataset is comprised of an input vector X_i ($i = 1, 2, 3$, representing the disk diameter, D, and J_c, respectively) and an output scalar variable Y representing the equilibrium value of $<m_z>$. The trained machine learning model can be used to rapidly regress the Y as a function of X_i. As one example, Fig. 4e shows the machine-learning-model predicted J_c vs. D switching diagram for the disk diameter of 40 nm, which is well consistent with the diagram calculated via micromagnetic simulations except one outlier (c.f., Fig. 4c). Remarkably, the machine-learning-predicted diagram, which also contains many more data points than the micromagnetic-simulations-based diagram, was calculated in <2 min in a laptop. This is much faster than that by micromagnetic simulations, where the calculation of one switching diagram takes ~250 groups of simulations and each group typically takes ~4 h to complete with 16 cores running simultaneously on state-of-the-art supercomputers. The prediction accuracy of our machine learning model is >90% with a mean square error of ~0.01 (Fig. 4f), and can be further improved with more training datasets. Such machine learning model is thus particularly suited for accelerating the prediction of such switching diagram, e.g., J_c vs. X (where X = disk size, D, K_{inter}, M_s, etc.), in which case large quantities of micromagnetic simulations are normally needed.

Having shown that the >90° perpendicular switching occurs through a deterministic nucleation and lateral growth of reversed domain (Fig. 2), we further perform ASD simulations to analyze the early-stage nucleation kinetics at which the embryos (clusters of several atoms) are too small to accurately describe with a continuum micromagnetic model. A multilayer stack (similar to the structure in Fig. 1a) with 50 nm diameter MgO/Co bilayer nanodisks on top of a Pt stripe is considered as the model system. There are two reasons for considering Co (instead of CoFeB) as the magnetic layer herein. First, since the goal is to reveal the nucleation and growth kinetics of the reversed domain (within which $m_z < 0$) at the atomic scale, a pure metal Co would be a better model system than the solid-solution CoFeB. Second, it will show that the proposed two-step switching is applicable to other ferromagnets.

We first present the micromagnetic simulations results on the >90° switching in Co as the baseline of the discussion. As shown in Fig. 5a, after a brief incubation period (during which $m_z > 0$), the volume fraction (V_r) of the reversed domain (within which $m_z < 0$) increases gradually from 0 to above 60% at saturation, when moderate charge currents are applied (the range of J_c is from 1.1×10^{13} to 1.5×10^{13} A/m^2). A larger J_c yields a larger out-of-plane torque τ_z^{tot} which in turn leads to faster nucleation (that is, shorter incubation period) and faster growth. Notably, the growth of the reversed domain (described by the evolution of V_r at later time stages) well fits the Kolmogorov–Avrami equation[38,39], given by $V_r = V_0(1 - e^{-(t/t_c)^n})$, where V_0 is a fitting parameter; t_c is the characteristic time for the V_r to saturate, which decreases from 0.24 to 0.12 ns as J_c increases; n is the effective dimension of domain growth and is best fitted with values around 2, indicating a two-dimensional domain growth as expected.

Figure 5b shows the nucleation and growth kinetics of reversed domain simulated using ASD modeling, where a 2D hexagonal lattice of 36,096 atoms is used to approximately describe the 1.1-nm-thick hcp Co nanodisk. The evolution of the average atomic spin moment and free energy terms during the entire two-step switching process are also simulated by ASD modeling (see Supplementary Fig. 7). As shown in Fig. 5b, the nucleation and growth of the reversed domain display generally similar kinetic features to those obtained using micromagnetic modeling. Specifically, the percentage of atoms (N_r) with flipped atomic spin moment ($S_z < 0$, see "Methods") displays a similar saturation value. The growth kinetics of the reversed domain can likewise be fitted using the Kolmogorov–Avrami equation. For early nucleation stage (0.055 ns), Fig. 5c shows the density maps of the perpendicular atomic spin moment S_z at three different nucleation clusters (labeled as P_1, P_2, and P_3, as indicated in Fig. 5d) at the same time stage. It can be seen that the switching is fastest at P_3 and then P_2, which is also indicated by the evolution trajectories of the atomic spin moment in the central atoms (marked by circles) at these three points from 0 to 0.06 ns (Fig. 5e). This locally variant switching speeds are mainly due to the fact that the downward-pointing effective SOT field, the magnitude of which is proportional to $|S_y|$, is the largest at cluster P_3 while smallest at P_1 at this early stage of nucleation. As a result, the magnetization at P_3 can be flipped more quickly.

In summary, we have computationally demonstrated a field-free SOT-mediated perpendicular magnetization switching, the implementation of which does not require any changes in the standard architecture of an SOT-MRAM cell, thus being promising for practical applications. The full 180° switching is achieved through a >90° perpendicular switching (m_z changes from ~1 to <0, or vice versa from approximately −1 to >0) plus a subsequent precession relaxation to the revered direction. The simulations indicate that there are two key critical steps for achieving the >90° perpendicular switching, including the nucleation of the reverse domain and its successful growth to exceed the critical "half-up half-down" spin state (e.g., Fig. 2c). Successful realization of both steps relies on striking the balance of the interfacial DMI, geometrical confinement, and SOT by tuning the interfacial DMI strength (D), lateral size of the magnetic layer, and magnitude of charge current density (J_c), respectively.

Our analyses show that the growth of the reversed domain is two-dimensional and can be well described by classical theory of growth kinetics, similarly to the growth of polarization domain in ferroelectric thin films[40]. Our ASD simulations, which resolve the evolution of magnetic moment in every single magnetic atom in a confined system, provide an atomistic picture of the nucleation kinetics of SOT-mediated perpendicular magnetization switching in general. Last but not the least, we have trained a decision-tree-based machine learning model using about 1000 groups of micromagnetic simulations that were benchmarked using the open-source micromagnetic simulation package MuMax3. This machine learning model along with the datasets can evolve to an accurate and efficient computational design tool that can be used to quickly determine whether the field-free switching can occur and what are the values of average magnetization at equilibrium under a given set of design parameters (D, size, J_c, key magnetic parameters, etc.).

METHODS

Micromagnetic simulations using μ-Pro

Most of the micromagnetic simulations in this work are performed using the commercial μ-Pro® package (mupro.co/contact), which is CPU (Central Processing Unit) based and parallelized using Message Passing Interface. Consider a MgO/$Co_{20}Fe_{60}B_{20}$(1.1)/Pt multilayer structure, where the CoFeB disk is discretized using a cuboid-shaped cell of 1 nm × 1 m × 0.55 nm. We note that the thickness of the CoFeB (1.1 nm) is significantly smaller than the magnetic exchange length $l_{ex} = \sqrt{A/(0.5\mu_0 M_s^2)} \sim 4.54$ nm, where A is the Heisenberg exchange coefficient, μ_0 is the vacuum permeability, M_s is saturation magnetization. In combination with the fact that the interfacial DMI field does not modify the gradient of magnetization along the thickness direction (shown later), we expect the magnetization distribution to be spatially uniform along the thickness direction, which is confirmed by micromagnetic simulations. The simulations performed using a smaller cell size along the z-axis (i.e., 0.275 nm) yield the same results. Other magnetic nanostructures with sufficiently strong room temperature PMA, which can arise due to either the magnetic interface anisotropy (e.g., 0.5-nm-thick $Fe_{80}Co_{20}$, ref. [41]) or the intrinsic magnetocrystalline anisotropy such as FePt[32], can also be used to demonstrate the proposed field-free SOT perpendicular magnetization switching.

The magnetization in each cell $\mathbf{M} = M_s\mathbf{m}$, where $\mathbf{m} = (m_x, m_y, m_z)$ is the normalized magnetization vector. The evolution of the normalized magnetization $\mathbf{m}$ is obtained through solving the Landau–Lifshitz–Gilbert (LLG) equation with an SOT term $\boldsymbol{\tau}^{SOT}$,

$$\frac{\partial \mathbf{m}}{\partial t} = \tau^{tot} = -\frac{\gamma_0}{1+\alpha^2}\left(\mathbf{m}\times\mathbf{H}_{eff} + \alpha\mathbf{m}\times\mathbf{m}\times\mathbf{H}_{eff}\right) + \tau^{SOT}, \quad (1)$$

where α is the Gilbert damping coefficient and γ_0 is the gyromagnetic ratio. The effective magnetic field $\mathbf{H}_{eff} = -\frac{1}{\mu_0 M_s}\frac{\delta F_{tot}}{\partial \mathbf{m}}$; $F_{tot} = \int f_{tot} dV$; the total magnetic free energy density $f_{tot} = f_{stray} + f_{anis} + f_{DMI} + f_{exch}$ is the sum of the densities of the magnetic stray field energy, perpendicular anisotropy energy, interfacial DMI energy, and Heisenberg exchange energy, respectively. Each energy density term is associated with an effective magnetic field. Therefore, one can also write $\mathbf{H}_{eff} = \mathbf{H}_{stray} + \mathbf{H}_{anis} + \mathbf{H}_{DMI} + \mathbf{H}_{exch}$. Among them, the magnetic stray field $\mathbf{H}_{stray}$ is obtained through solving magnetostatic equilibrium equation $\nabla \cdot \mu_0(\mathbf{H}_{stray} + \mathbf{M}) = 0$ under a finite-size boundary condition, using a Fast Fourier Transform accelerated convolution theorem[42]. The anisotropy field $\mathbf{H}_{anis} = -\frac{1}{\mu_0 M_s}\frac{\partial f_{anis}}{\partial \mathbf{m}}$, where the uniaxial magnetic anisotropy energy density $f_{anis} = \frac{K_{inter}}{d}(1 - m_z^2)$. For the ultrathin (1.1-nm thick) CoFeB in this work, it is the contribution from the magnetic interface anisotropy $\frac{K_{inter}}{d}$ that outweighs the out-of-plane shape anisotropy K_{shape}^{OOP}. The latter can be evaluated based on numerically calculated out-of-plane stray field. Experimentally, a room temperature thermally stable perpendicular magnetization has been demonstrated in ultrathin (1.3 nm or thinner) CoFeB nanodisks with diameter as small as 40 nm[28] (down to 20 nm according to a very recent report[43]), where MgO is used as the overlayer, the same as in our structure. The interfacial DMI field $\mathbf{H}_{DMI} = \frac{2D}{\mu_0 M_s}\left(\frac{\partial m_z}{\partial x}, \frac{\partial m_z}{\partial y}, -\frac{\partial m_x}{\partial x} - \frac{\partial m_y}{\partial y}\right)$, where D is the strength of the interfacial DMI[24]. When calculating the $\mathbf{H}_{DMI}$ in a geometrically confined nanostructure, the boundary condition $\frac{\partial \mathbf{m}}{\partial \mathbf{n}} = \frac{D}{2A}((\mathbf{n}\times e_z)\times\mathbf{m})$ needs to be applied at the interface between the magnetic disk and nonmagnetic phase[24], where $\mathbf{n}$ is the interface normal; e_z is the unit vector along the z-direction. The Heisenberg exchange field $\mathbf{H}_{exch} = \frac{2A}{\mu_0 M_s}\nabla^2\mathbf{m}$. The influence of thermal fluctuations is modeled by adding a thermal fluctuation field $\mathbf{H}_{therm}$ to $\mathbf{H}_{eff}$, given by $\mathbf{H}_{therm} = \eta\sqrt{\frac{2\alpha k_B T}{\mu_0 M_s \gamma_0 \Delta V \Delta t}}$, where k_B is the Boltzmann constant, $T = 298$ K is the temperature, ΔV is the volume of each simulation cell, Δt is the time interval in real unit. $\boldsymbol{\eta} = \boldsymbol{\eta}(\mathbf{r}, t) = (\eta_x, \eta_y, \eta_z)$, where η_x, η_y, η_z are Gaussian-distributed random number with a mean of zero, which are uncorrelated both in space and time.

Let us further consider that the input charge current flowing along the $-y$ direction ($J_{c,-y}$) of the Pt layer. Due to the SHE[3], electrons with opposite spin orientations are deflected transversely towards the top and bottom surfaces along the z-axis (yielding a spin current, denoted as $J_{s,z}$) as well as the two lateral surfaces along the x-axis (yielding a spin current $J_{s,x}$). We note that the spin current is a flow of angular momentum, and that the net charge currents along both x and z are zero. Since the magnetic nanodisk is laid on the top surface of the Pt layer, only the z-axis spin current $J_{s,z}$, which has a spin polarization $\boldsymbol{\sigma}$ along x according to the right-hand rule of the SHE[3], can be injected into the nanomagnet (Fig. 1a). In this case, the transfer of angular momentum from the Pt to nanomagnet can only occur along the z-axis, and in turn switch the magnetization in the latter via the SOT[44]. Experimental demonstration of this switching scheme can be found in for example refs. [8,9,15,45]. The spin–orbit torque $\boldsymbol{\tau}^{SOT}$ is expressed as[8,25,26],

$$\tau^{SOT} = -\frac{\gamma_0}{1+\alpha^2}\left(\left(\mathbf{m}\times\mathbf{H}^{SOT}\right) - \alpha\mathbf{H}^{SOT}\right), \quad (2)$$

where the corresponding effective field $\mathbf{H}^{SOT} = H_0(\mathbf{m}\times\boldsymbol{\sigma}_{s,x})$. Here, the

prefactor $H_0 = \frac{\mu_B J_c \theta_{SH}}{\gamma_0 e d M_s}$, where μ_B is the Bohr magneton; J_c is the density of the charge current; θ_{SH} is the spin hall angle, e is the elementary charge, and d is the thickness of CoFeB layer. Therefore, the z-component of the $\boldsymbol{\tau}^{SOT}$ is given by $\tau_z^{SOT} = -\gamma_0 H_0 m_x m_z$, while the z-component of the $\mathbf{H}^{SOT}$ is $H_z^{SOT} = -H_0 m_y$. In an initially $+z$ magnetized disk ($m_z > 0$) with inward tilted magnetization (see Fig. 2a), the τ_z^{SOT} and H_z^{SOT} are both negative only in the bottom left region of the disk, where $m_x > 0$ and $m_y > 0$ (Fig. 2f) under the application of a positive J_c, leading to the nucleation of $-z$ magnetized domain therein.

The LLG equation is solved using forth-order Runge–Kutta method, with a dimensionless discretized time interval $\Delta t^* = \frac{\gamma_0 M_s}{1+\alpha^2}\Delta t = 0.005$. Our simulation results are the same if using a smaller reduced time step of 0.0025. The material parameters used for micromagnetic simulations are listed as follows. For 1.1-nm-thick $Co_{20}Fe_{60}B_{20}$: $M_s = 1.21 \times 10^6$ A/m, $\alpha = 0.027$, $K_{inter} = 1.3 \times 10^{-3}$ J/m^2 ref. [28]; $\gamma_0 = 2.265 \times 10^5$ Hz/(A/m) ref. [46]; $A = 1.9 \times 10^{-11}$ J/m ref. [47]; $\theta_{SH} = 0.0812$ ref. [48]; For 1.1-nm-thick Co, $M_s = 1.40 \times 10^6$ A/m, $K_{inter} = 1.6 \times 10^{-3}$ J/m^3, $A = 2.75 \times 10^{-11}$ J/m, $D = 2.05 \times 10^{-3}$ J/m^2 ref. [49]; $\alpha = 0.31$ ref. [50], $\gamma_0 = 2.21 \times 10^5$ Hz/(A/m) ref. [51].

Micromagnetic simulation using MuMax3

We used MuMax3, which is GPU (Graphics Processing Unit) based, to validate the micromagnetic simulation results from the μ-Pro package. The results obtained from both packages are well consistent (e.g., see Figs. 1 and 3). In MuMax3, the spin torque term $\boldsymbol{\tau}^{SL}$ is Slonczewski type, given as[52],

$$\tau^{SL} = \beta \frac{\epsilon - \alpha\epsilon\prime}{1+\alpha^2}(\mathbf{m} \times (\sigma \times \mathbf{m})) - \beta \frac{\epsilon\prime - \alpha\epsilon}{1+\alpha^2}(\mathbf{m} \times \sigma), \tag{3}$$

where $\beta = \frac{J_c \hbar}{M_s m_e d\prime}$, $\epsilon = \frac{\theta_{SH}\Lambda^2}{(\Lambda^2+1)+(\Lambda^2-1)(\mathbf{m}\cdot\sigma)}$. By setting $\Lambda = 1$, $\epsilon\prime = 0$, the expression of $\boldsymbol{\tau}_{SL}$ in Eq. (3) can be written as,

$$\tau^{SL} = \frac{\beta\theta_{SH}}{2(1+\alpha^2)}((\mathbf{m} \times (\sigma \times \mathbf{m})) - \alpha(\sigma \times \mathbf{m})). \tag{4}$$

Given that $\mu_B = \frac{e\hbar}{2m_e}$, the expression of $\boldsymbol{\tau}^{SL}$ is the same as that of $\boldsymbol{\tau}^{SOT}$ in Eq. (2). This allows us to model the SOT switching using MuMax3.

Machine learning the switching diagram

The 1069 groups of micromagnetic simulation datasets comprised of tabulated $\{X_i, Y\}$ are divided into 989 training groups and 80 testing groups, where X_i ($i = 1, 2, 3$) refers to the disk diameter, interfacial DMI strength D, and the charge current J_c; the scalar variable Y refers to the $\langle m_z \rangle$ at equilibrium. Ten different machine learning models that are available in Scikit-learn[53] (including linear regression, Gaussian process regression, polynomial regression, etc.) were separately trained to regress Y as a function of X_i. Among them, the decision-tree regression model delivers the highest accuracy. The accuracy is represented by R^2 score.

$$R^2 \equiv 1 - \frac{\sum_i (y_i - f_i)^2}{\sum_i (y_i - \bar{y})^2} \tag{5}$$

where y and f are the $\langle m_z \rangle$ calculated from micromagnetic simulation and machine learning, respectively.

Atomistic spin dynamics (ASD) simulations

The ASD simulations are performed using our in-house package called AtomMag (under development) which has both a GPU-accelerated and a CPU-based version. The physical validity of AtomMag is tested by making comparison to Fidimag[54], an existing open-source ASD simulation package. The testing results are summarized in Supplementary Fig. 8. Consider a MgO/Co/Pt multilayer structure, where the Co disk is described by arranging 36,096 atoms in a 2D hexagonal lattice with lattice parameters $a = 2.5$ Å, corresponding to a 50-nm disk diameter. The magnetic moment of each atom is given as $\boldsymbol{\mu}_i = \mu_s \mathbf{S}_i$ ($i = 1, 2 \ldots 36{,}096$), where $\mathbf{S}_i$ is the unit vector of the atomic spin and μ_s is the magnitude of spin magnetic moment. The evolution of the unit spin direction $\mathbf{S}_i$ is obtained through solving the atomistic LLG Equation with a spin–orbit torque term $\boldsymbol{\tau}_{SOT}^i$,

$$\frac{\partial \mathbf{S}_i}{\partial t} = -\frac{\gamma}{1+\alpha^2}\left(\mathbf{S}_i \times \mathbf{B}_{eff}^i + \alpha \mathbf{S}_i \times \mathbf{S}_i \times \mathbf{B}_{eff}^i\right) + \tau_{SOT}^i, \tag{6}$$

where α is the Gilbert damping coefficient and $\gamma = \gamma_0/\mu_0$ is the gyromagnetic ratio. The effective magnetic field at each atom site $\mathbf{B}_{eff}^i = -\frac{1}{\mu_s}\frac{\partial \mathcal{H}_{tot}}{\partial \mathbf{S}_i} + \mathbf{B}_{therm}^i$, where $\mathcal{H}$ is the total spin Hamiltonian; $\mathcal{H}_{tot} = \mathcal{H}_{dipole} + \mathcal{H}_{anis} + \mathcal{H}_{DMI} + \mathcal{H}_{exch}$ is the sum of the Hamiltonians of magnetic dipole–dipole interaction, uniaxial magnetic anisotropy, interface DMI and Heisenberg exchange interaction of all atoms. Since each Hamiltonian is associated with an effective magnetic field, one can write $\mathbf{B}_{eff}^i = \mathbf{B}_{dipole}^i + \mathbf{B}_{anis}^i + \mathbf{B}_{DMI}^i + \mathbf{B}_{exch}^i + \mathbf{B}_{therm}^i$[55]. Among them,

$$\mathbf{B}_{dipole}^i = \frac{\mu_0 \mu_s}{4\pi} \sum_{j \neq i} \frac{3(\mathbf{S}_j \cdot \hat{\mathbf{r}}_{ij})\hat{\mathbf{r}}_{ij} - \mathbf{S}_j}{r_{ij}^3}, \tag{7}$$

where r_{ij} is the distance between atom site i and atom site j, $\hat{\mathbf{r}}_{ij}$ is the unit vector along the direction of $\mathbf{r}_{ij} = \mathbf{r}_j - \mathbf{r}_i$.

$$\mathbf{B}_{anis}^i = \frac{2K_0}{\mu_s}(\mathbf{S}_i \cdot \mathbf{u})\mathbf{u}, \tag{8}$$

where K_0 is the anisotropy constant, $\mathbf{u}$ is the direction vector of the magnetic easy axis.

$$\mathbf{B}_{DMI}^i = \frac{1}{\mu_s}\sum_i \mathbf{D}_{ij} \times \mathbf{S}_j, \tag{9}$$

where $\mathbf{D}_{ij}$ is the Dzyaloshinskii–Moriya vector between two neighboring spins at atom site i and j. For interfacial DMI, $\mathbf{D}_{ij} = D_0 \hat{z} \times \mathbf{r}_{ij}$, where D_0 is the interfacial DMI constant.

$$\mathbf{B}_{exch}^i = \frac{J_{ij}}{\mu_s}\sum_j \mathbf{S}_j, \tag{10}$$

where J_{ij} is the exchange parameter describing the Heisenberg-type exchange coupling between two spins at atom site i and j. For hexagonal Co, first-principles calculations indicate that the second nearest-neighbor exchange parameter is negligibly small[56]. Therefore, the summation in Eq. (10) is truncated to include the nearest-neighbor exchange coupling only.

Furthermore, the thermal fluctuation field $\mathbf{B}_{therm}^i$ is given by[57],

$$\mathbf{B}_{therm}^i = \beta\sqrt{\frac{2\alpha k_B T}{\mu_s \gamma \Delta t}}. \tag{11}$$

Similarly to the above-described micromagnetic model, the Gaussian-distributed stochastic vector $\boldsymbol{\eta} = \eta(\mathbf{r}, t) = (\eta_x, \eta_y, \eta_z)$ is generated via Box–Muller transform of the uniformly distributed random numbers. The latter is generated using the high-performance GPU-accelerated random number generator cuRAND. In contrast to the fact that the peak amplitude of the thermal fluctuation field in a micromagnetic model is dependent on the size of the simulation cell, the thermal fluctuation field is directly applied to every single spin in ASD modeling. Therefore, temperature-dependent magnetic properties (e.g., see refs. [58,59]) can be accurately modeled via ASD simulations. In this work, the main purpose of performing ASD simulations is to more accurately model the early-stage nucleation kinetics (Fig. 5b–e), e.g., in which area the spins flip the fastest? What is the intrinsic time scale of nucleation? To address these questions, $\mathbf{B}_{therm}^i$ is not included, otherwise the associated fluctuation on every atomic spin will obscure the analysis. Finally, the SOT $\boldsymbol{\tau}_{SOT}^i$ is expressed as[60],

$$\tau_{SOT}^i = \beta_{FL}\mathbf{S}_i \times \sigma + \beta_{DL}\mathbf{S}_i \times (\mathbf{S}_i \times \sigma), \tag{12}$$

where β_{FL} is the strength of field-like torque term, β_{DL} is the strength of damping-like torque, $\boldsymbol{\sigma}$ is the orientation of spin polarization, which is along $+x$ direction in our case.

The parameters in ASD simulations can be derived from their continuum-scale counterparts used in micromagnetic simulations as follows:[61] $J = \frac{2a_z A}{\sqrt{3}} = 1.27 \times 10^{-20}$ J, $D_0 = \frac{a a_z D}{\sqrt{3}} = 1.18 \times 10^{-22}$ J, $\mu_s = \frac{\sqrt{3}}{2}a^2 a_z M_s = 3.03 \times 10^{-23}$ J/T, $K_0 = \frac{\sqrt{3}}{2}a^2 a_z K = 3.14 \times 10^{-23}$ J, where $a_z = 4.0$ Å. Note that these continuum-scale parameters (A, D, M_s, K) are values experimentally measured for 1.1-nm-thick Co film. Here, we are considering a 2D hexagonal lattice with a thickness of only one monolayer (~ 4.0 Å) for reducing the computational cost (which is common for ASD simulations[60,61]), by assuming the variation of magnetization along the thickness direction is negligible. This approximation would lead to significantly stronger demagnetization (dipolar) field in the system than it is supposed to be in a 1.1-nm-thick Co sample, which in turn reduce the PMA. To balance the stronger demagnetization field, we use a larger anisotropy constant $K_0 = 5.50 \times 10^{-23}$ J. It is shown that under this combination of parameters, the extent of edge magnetization tilting ($m_{IP} \sim 0.3$, c.f., Fig. 4b) is the same as that in the micromagnetic simulations of 1.1-nm-thick Co film. Strength of field-like torque and damping-like torque is proportional to

the magnitude of charge current density J_c: $\beta_{FL} = \frac{a}{1+a^2}\frac{\mu_B \theta_{SH}}{edM_s} J_c$, $\beta_{DL} = -\frac{1}{1+a^2}\frac{\mu_B \theta_{SH}}{edM_s} J_c$, the pre-factors are derived corresponding to the SOT term of micromagnetic LLG equation. The LLG equation is solved using forth-order Runge–Kutta method with a time interval of 1 fs. Using a smaller time interval of 0.5 fs yields the same results.

DATA AVAILABILITY

The data that support the plots presented in this paper and its supplemental information files are available from the corresponding authors upon reasonable request. All training data for the machine learning model can be accessed via https://github.com/mdai26/ML-SOT.

CODE AVAILABILITY

The in-house open-source AtomMag package for performing the atomistic spin dynamics simulations can be accessed via https://github.com/jhu238/AtomMag. Open-source codes for the machine learning model can be accessed via https://github.com/mdai26/ML-SOT.

Received: 7 March 2020; Accepted: 22 May 2020;
Published online: 12 June 2020

REFERENCES

1. Oboril, F., Bishnoi, R., Ebrahimi, M. & Tahoori, M. B. Evaluation of hybrid memory technologies using SOT-MRAM for on-chip cache hierarchy. *IEEE Trans. Comput. Des. Integr. Circuits Syst.* **34**, 367–380 (2015).
2. Li, X., Lee, A., Razavi, S. A., Wu, H. & Wang, K. L. Voltage-controlled magnetoelectric memory and logic devices. *MRS Bull.* **43**, 970–977 (2018).
3. Hirsch, J. E. Spin Hall effect. *Phys. Rev. Lett.* **83**, 1834–1837 (1999).
4. Valenzuela, S. O. & Tinkham, M. Direct electronic measurement of the spin Hall effect. *Nature* **442**, 176–179 (2006).
5. Zhang, W. et al. Spin hall effects in metallic antiferromagnets. *Phys. Rev. Lett.* **113**, 1–6 (2014).
6. Miron, I. M. et al. Perpendicular switching of a single ferromagnetic layer induced by in-plane current injection. *Nature* **476**, 189–193 (2011).
7. Liu, L. et al. Spin-torque switching with the giant spin Hall effect of tantalum. *Science* **336**, 555–558 (2012).
8. Fukami, S., Anekawa, T., Zhang, C. & Ohno, H. A spin-orbit torque switching scheme with collinear magnetic easy axis and current configuration. *Nat. Nanotechnol.* **11**, 621–625 (2016).
9. Yu, G. et al. Switching of perpendicular magnetization by spin-orbit torques in the absence of external magnetic fields. *Nat. Nanotechnol.* **9**, 548–554 (2014).
10. Yu, G. et al. Current-driven perpendicular magnetization switching in Ta/CoFeB/[TaOxor MgO/TaOx] films with lateral structural asymmetry. *Appl. Phys. Lett.* **105**, 102411 (2014).
11. Chen, T. Y., Chan, H. I., Liao, W. B. & Pai, C. F. Current-induced spin-orbit torque and field-free switching in Mo-based magnetic heterostructures. *Phys. Rev. Appl.* **10**, 1 (2018).
12. Lau, Y. C., Betto, D., Rode, K., Coey, J. M. D. & Stamenov, P. Spin-orbit torque switching without an external field using interlayer exchange coupling. *Nat. Nanotechnol.* **11**, 758–762 (2016).
13. Zhao, Z., Smith, A. K., Jamali, M. & Wang, J. P. External-field-free spin Hall switching of perpendicular magnetic nanopillar with a dipole-coupled composite. *Struct. Adv. Electron. Mater.* **1901368**, 1–9 (2020).
14. Fukami, S., Zhang, C., Duttagupta, S., Kurenkov, A. & Ohno, H. Magnetization switching by spin-orbit torque in an antiferromagnet-ferromagnet bilayer system. *Nat. Mater.* **15**, 535–541 (2016).
15. Cai, K. et al. Electric field control of deterministic current-induced magnetization switching in a hybrid ferromagnetic/ferroelectric structure. *Nat. Mater.* **16**, 712–716 (2017).
16. Wang, Q. et al. Strain-mediated spin-orbit-torque switching for magnetic. *Mem. Phys. Rev. Appl.* **10**, 034052 (2018).
17. Ma, Q. et al. Switching a perpendicular ferromagnetic layer by competing spin currents. *Phys. Rev. Lett.* **120**, 117703 (2018).
18. Wang, M. et al. Field-free switching of a perpendicular magnetic tunnel junction through the interplay of spin–orbit and spin-transfer torques. *Nat. Electron.* **1**, 582–588 (2018).
19. You, L. et al. Switching of perpendicularly polarized nanomagnets with spin orbit torque without an external magnetic field by engineering a tilted anisotropy. *Proc. Natl Acad. Sci. USA* **112**, 10310–10315 (2015).
20. Wang, Z. et al. Field-free spin–orbit-torque switching of perpendicular magnetization aided by uniaxial shape anisotropy. *Nanotechnology* **30**, 375202 (2019).
21. Chen, B., Lourembam, J., Goolaup, S. & Lim, S. Ter. Field-free spin-orbit torque switching of a perpendicular ferromagnet with Dzyaloshinskii-Moriya interaction. *Appl. Phys. Lett.* **114**, 022401 (2019).
22. Wu, K., Su, D., Saha, R. & Wang, J.-P. Deterministic field-free switching of a perpendicularly magnetized ferromagnetic layer via the joint effects of the Dzyaloshinskii–Moriya interaction and damping- and field-like spin–orbit torques: an appraisal. *J. Phys. D. Appl. Phys.* **53**, 205002 (2020).
23. Tacchi, S. et al. Interfacial Dzyaloshinskii-Moriya interaction in Pt/CoFeB films: effect of the heavy-metal thickness. *Phys. Rev. Lett.* **118**, 1–6 (2017).
24. Rohart, S. & Thiaville, A. Skyrmion confinement in ultrathin film nanostructures in the presence of Dzyaloshinskii-Moriya interaction. *Phys. Rev. B.* **88**, 184422 (2013).
25. Mikuszeit, N. et al. Spin-orbit torque driven chiral magnetization reversal in ultrathin nanostructures. *Phys. Rev. B* **92**, 1–5 (2015).
26. Martinez, E. et al. Universal chiral-triggered magnetization switching in confined nanodots. *Sci. Rep.* **5**, 1–15 (2015).
27. Baumgartner, M. et al. Spatially and time-resolved magnetization dynamics driven by spin-orbit torques. *Nat. Nanotechnol.* **12**, 980–986 (2017).
28. Ikeda, S. et al. A perpendicular-anisotropy CoFeB-MgO magnetic tunnel junction. *Nat. Mater.* **9**, 721–724 (2010).
29. Kanai, S., Matsukura, F. & Ohno, H. Electric-field-induced magnetization switching in CoFeB/MgO magnetic tunnel junctions with high junction resistance. *Appl. Phys. Lett.* **108**, 192406 (2016).
30. Grezes, C. et al. Ultra-low switching energy and scaling in electric-field-controlled nanoscale magnetic tunnel junctions with high resistance-area product. *Appl. Phys. Lett.* **108**, 012403 (2016).
31. Nowak, J. J. et al. Dependence of voltage and size on write error rates in spin-transfer torque magnetic random-access memory. *IEEE Magn. Lett.* **7**, 4–7 (2016).
32. Yi, M., Zhang, H. & Xu, B. X. Voltage-driven charge-mediated fast 180 degree magnetization switching in nanoheterostructure at room temperature. *npj Comput. Mater.* **3**, 1–8 (2017).
33. Hu, J.-M., Yang, T. & Chen, L.-Q. Strain-mediated voltage-controlled switching of magnetic skyrmions in nanostructures. *npj Comput. Mater.* **4**, 62 (2018).
34. Hu, J. M. et al. Fast magnetic domain-wall motion in a ring-shaped nanowire driven by a voltage. *Nano Lett.* **16**, 2341–2348 (2016).
35. Bisig, A. et al. Correlation between spin structure oscillations and domain wall velocities. *Nat. Commun.* **4**, 1–8 (2013).
36. Nakatani, Y., Thiaville, A. & Miltat, J. Faster magnetic walls in rough wires. *Nat. Mater.* **2**, 521–523 (2003).
37. Schryer, N. L. & Walker, L. R. The motion of 180° domain walls in uniform dc magnetic fields. *J. Appl. Phys.* **45**, 5406–5421 (1974).
38. Ishibashi, Y. & Takagi, Y. Note on ferroelectric domain switching. *J. Phys. Soc. Jpn.* **31**, 506–510 (1971).
39. Ishibashi, Y. Theory of polarization reversals in ferroelectrics based on landau-type free energy. *Jpn. J. Appl. Phys.* **31**, 2822–2824 (1992).
40. Nelson, C. T. et al. Domain dynamics during ferroelectric switching. *Science* **334**, 968–971 (2011).
41. Nozaki, T., Shiota, Y., Shiraishi, M., Shinjo, T. & Suzuki, Y. Voltage-induced perpendicular magnetic anisotropy change in magnetic tunnel junctions. *Appl. Phys. Lett.* **96**, 022506 (2010).
42. Fabian, K. et al. Three-dimensional micromagnetic calculations for magnetite using FFT. *Geophys. J. Int.* **124**, 89–104 (1996).
43. Jinnai, B., Watanabe, K., Fukami, S. & Ohno, H. Scaling magnetic tunnel junction down to single-digit nanometers—challenges and prospects. *Appl. Phys. Lett.* **116**, 160501 (2020).
44. Brataas, A., Kent, A. D. & Ohno, H. Current-induced torques in magnetic materials. *Nat. Mater.* **11**, 372–381 (2012).
45. Liu, L., Moriyama, T., Ralph, D. C. & Buhrman, R. A. Spin-torque ferromagnetic resonance induced by the spin Hall effect. *Phys. Rev. Lett.* **106**, 1–4 (2011).
46. Maruyama, T. et al. Large voltage-induced magnetic anisotropy change in a few atomic layers of iron. *Nat. Nanotechnol.* **4**, 158–161 (2009).
47. Sato, H. et al. CoFeB thickness dependence of thermal stability factor in CoFeB/MgO perpendicular magnetic tunnel junctions. *IEEE Magn. Lett.* **3**, 1–4 (2012).
48. Nan, T. et al. A strain-mediated magnetoelectric-spin-torque hybrid structure. *Adv. Funct. Mater.* **29**, 1–8 (2019).
49. Boulle, O. et al. Room-temperature chiral magnetic skyrmions in ultrathin magnetic nanostructures. *Nat. Nanotechnol.* **11**, 449–454 (2016).
50. Metaxas, P. J. et al. Creep and flow regimes of magnetic domain-wall motion in ultrathin Pt/Co/Pt films with perpendicular anisotropy. *Phys. Rev. Lett.* **99**, 1–4 (2007).
51. Bauer, D. *Atomistic Spin-dynamics in Confined Magnetic Nano-structures*. Doctoral dissertation, Diploma thesis, RWTH Aachen (2008).
52. Vansteenkiste, A. et al. The design and verification of MuMax3. *AIP Adv.* **4**, 107133 (2014).

53. Pedregosa, F. et al. Scikit-learn: machine learning in Python. *J. Mach. Learn. Res.* **12**, 2825–2830 (2011).
54. Bisotti, M.-A. et al. Fidimag – a finite difference atomistic and micromagnetic simulation package. *J. Open Res. Softw*. **6**, 22 (2018).
55. Eriksson, O., Bergman, A., Bergqvist, L. & Hellsvik, J. *Atomistic Spin Dynamics: Foundations and Applications* (Oxford university press, Oxford, 2017).
56. Sabiryanov, R. F. & Jaswal, S. S. Magnons and magnon-phonon interactions in Iron. *Phys. Rev. Lett.* **83**, 2062–2064 (1999).
57. Evans, R. F. L. et al. Atomistic spin model simulations of magnetic nanomaterials. *J. Phys. Condens. Matter* **26**, 103202 (2014).
58. Gong, Q., Yi, M., Evans, R. F. L., Xu, B. X. & Gutfleisch, O. Calculating temperature-dependent properties of Nd2Fe14 B permanent magnets by atomistic spin model simulations. *Phys. Rev. B* **99**, 1–11 (2019).
59. Gong, Q., Yi, M. & Xu, B. X. Multiscale simulations toward calculating coercivity of Nd-Fe-B permanent magnets at high temperatures. *Phys. Rev. Mater.* **3**, 84406 (2019).
60. Ritzmann, U. et al. Trochoidal motion and pair generation in skyrmion and antiskyrmion dynamics under spin–orbit torques. *Nat. Electron.* **1**, 451–457 (2018).
61. Cortés-Ortuño, D. et al. Thermal stability and topological protection of skyrmions in nanotracks. *Sci. Rep.* **7**, 1–13 (2017).

ACKNOWLEDGEMENTS

The work is supported by a start-up fund from the University of Wisconsin–Madison. The simulations were performed using Bridges at the Pittsburgh Supercomputing Center through allocation TG-DMR180076, which is part of the Extreme Science and Engineering Discovery Environment (XSEDE) and supported by NSF grant ACI-1548562.

AUTHOR CONTRIBUTIONS

J.-M.H. conceived the idea, designed and supervised the research. M.D. performed the research. Both authors analyzed the data and wrote the paper.

COMPETING INTERESTS

The authors declare no competing interests.

ADDITIONAL INFORMATION

Supplementary information is available for this paper at https://doi.org/10.1038/s41524-020-0347-0.

Correspondence and requests for materials should be addressed to J.-M.H.

Reprints and permission information is available at http://www.nature.com/reprints

Publisher's note Springer Nature remains neutral with regard to jurisdictional claims in published maps and institutional affiliations.